

SYNTHESIS AND CHARACTERIZATION OF CARBON MAGNETIC NANOPARTICLES

by

SUNILSINGH GUSAIN

Presented to the Faculty of the Graduate School of
The University of Texas at Arlington in Partial Fulfillment
of the Requirements
for the Degree of

MASTER OF SCIENCE IN MATERIALS SCIENCE AND ENGINEERING

THE UNIVERSITY OF TEXAS AT ARLINGTON

May 2011

Copyright © by Sunilsingh Gusain 2011

All Rights Reserved

ACKNOWLEDGMENTS

I would like to express sincere gratitude to Dr. Ali R.Koymen, my research advisor, for his excellent guidance and constant encouragement throughout the research work. I would also like to thank Dr. Yaowu Hao and Dr. Samerandra Mohanty for their participation in my dissertation committee. I appreciate the support from Dr. Jiechao C. Jiang and Dr. Muhammed Yousufuddin. I am thankful to Dr. Maria Hossu, Rakesh Pratapbhai Chaudary, and Ajani Ross. Saurabh Mukherjee has been helpful. I am thankful to Physics and Material Science and Engineering Department staff for their support.

I am thankful to my friends Rishi Wadhwa, Kunal Tiwari, Kartik Shastry, Somil Rathi for their moral support and help. I would like to express sincere appreciation to my mother, sister and brother for their persistent support and encouragement.

March 2, 2010

ABSTRACT

SYNTHESIS AND CHARACTERIZATION OF CARBON MAGNETIC NANOPARTICLES

Sunilsingh Gusain, M.S.

The University of Texas at Arlington, 2010

Supervising Professor: Dr. Ali R. Koymen

Carbon incorporated iron nanoparticles (Fe-CNPs) were successfully synthesized using ultrasonic cavitation in Benzene. This novel method of carbon nanoparticle (CNP) synthesis is a very cost-effective and versatile as one can easily tune the microstructure and magnetic properties by varying few parameters, for e.g. voltage. The Fe-CNP complexes are produced due to the electric plasma discharge generated between the electrodes in an ultrasonic cavitation field of liquid benzene. The constituent of the CNPs can be easily modified by different choice of electrode materials- iron and graphite. The resultant Fe-CNPs were characterized by high-resolution transmission electron microscopy and X-ray photoelectron spectroscopy to reveal the presence of different forms of carbon and iron carbide particles. TEM results of Fe-CNP and CNP show lattice fringe and a diffraction pattern suggesting crystalline form of carbon form. Raman spectroscopy of Fe-CNPs shows similarity to that of diamond powder thus suggesting that the crystallinity of the samples can be easily varied as well. The

magnetic properties were investigated using superconducting quantum interference measurement devise (SQUID). The Fe-CNP show zero coercivity and increase in saturation magnetization with increase in synthesis voltage. On the other hand, the CNP produced using graphite electrodes are found to be magnetic in nature. Chemical analysis shows that the Fe-CNPs have iron constituent of ~3%. Biological applications of Fe-CNPs have been discussed.

TABLE OF CONTENTS

ACKNOWLEDGMENTS.....	iii
ABSTRACT	iv
LIST OF ILLUSTRATIONS.....	viii
LIST OF TABLES.....	x

Chapter	Page
1. INTRODUCTION	1
2. BACKGROUND INFORMATION AND LITERATURE REVIEW	4
2.1 Introduction to magnetism.....	4
2.1.1 Basics of Magnetism	4
2.1.2 Classes of Magnetic materials.....	5
2.1.3 Various energy terms.....	8
2.1.4 Effect of particle size on magnetic property	9
2.2 Literature review on synthesis of carbon magnetic nanoparticles.....	13
3. SYNTHESIS AND CHARACTERIZATION METHODS.....	15
3.1 Experimental setup.....	15
3.2 Magnetic characterization	17
3.2.1 Magnetic Property Measurement System Superconducting Quantum Interference Device (MPMS-SQUID)	17

3.3 Microstructure characterization	20
3.3.1 Transmission electron microscope (XPS)	20
3.4 Raman Spectroscopy.....	21
3.5 X-ray Photoelectron spectroscopy (XPS)	22
4. RESULTS AND DISCUSSIONS	24
4.1 Fe-CNP synthesized at 3.7 kV using iron electrodes.....	24
4.2 Fe-CNP synthesized at 4.1 kV using iron electrodes.....	27
4.3 CNP synthesized at 4.1 kV using graphite electrodes	35
5. CONCLUSION.....	41
REFERENCES.....	43
BIOGRAPHICAL INFORMATION	46

LIST OF ILLUSTRATIONS

Figure	Page
1.1 Schematic of nanoparticle drug complex represents a complex with magnetic core and decorated with drug and hydrophilic group.....	2
2.1 Illustration of a magnetic moment due to a current carrying loop	4
2.2 Effect on the magnetization (M) of an applied magnetic field (H) on (a) a paramagnetic system and (b) a diamagnetic system.....	5
2.3 Microscopic view of the domains in a ferromagnetic material.....	7
2.4 Magnetization behavior of a ferromagnet with an applied field	8
2.5 Change in hysteresis loop with change in particle size for single domain particle, multi domain particle and superparamagnetic particle.....	10
2.6 Hysteresis loop for multidomain (MD) and single domain (SD).....	11
2.7 Hysteresis curve of superparamagnetic particles	12
3.1 Schematics of acoustic pressure, liquid density and the bubble formation followed by ultrasonic cavitation.....	15
3.2 Schematic diagram of experimental setup.....	16
3.3 Setup for MPMS SQUID magnetometer	19
3.4 Transmission electron microscope	20
3.5 Schematics of Raman process	22
3.6 Schematic of X-ray Photoelectron Spectroscopy depicting the incident X-ray and the emitted photoelectrons.....	23
4.1 Hysteresis curve for sample produced with iron electrode at 3.7 KV ..	25
4.2 HRTEM image of Fe-CNP synthesized at 3.7 kV using iron electrodes	26

4.3 Raman spectrum of carbon nanoparticles synthesized at 3.7 kV using iron electrodes.....	27
4.4 Hysteresis curve for Fe-CNP produced with iron electrode at 4.1 kV.....	28
4.5 Comparison of Fe-CNP produced at 3.7 kV and 4.1kV	29
4.6 Elemental characterization of Fe-CNP synthesized using iron electrodes and at 4.1 kV.....	30
4.7 HRTEM image of Fe-CNP synthesized at 4.1kV using iron electrodes.....	31
4.8 HRTEM image of Fe-CNP synthesized at 4.1 kV	32
4.9 Selected area diffraction pattern of Fe-CNP synthesized at 4.1 kV	33
4.10 Raman spectroscopy using (a) blue and (b) red Laser of Fe-CNP synthesized at 4.1kV	34
4.11 X-ray diffraction of carbon nanoparticles synthesized with iron electrodes at 4.1kV	35
4.12 Hysteresis curve for CNP produced with graphite electrode at 4.1kV	36
4.13 HRTEM image of carbon nanoparticles synthesized at 4.1kV using graphite electrodes.....	37
4.14 Diffraction pattern of CNP prepared at 4.1kV with graphite electrodes	38
4.15 X-ray photoelectron spectroscopy of the nanoparticles synthesized using carbon electrodes.....	39
4.16 Raman spectroscopy of CNP synthesized at 4.1kV using graphite electrodes.....	40

LIST OF TABLES

Table	Page
2.1 Magnetic susceptibility of some common materials	6
4.1 Summary of the Energy dispersive X-ray analysis as shown in Figure 4.6.....	30
4.2 d-spacing as calculated from Figure 4.9.....	33
4.3 Tabulated value of the d-spacing as calculated from Figure 4.14.....	38
5.1 Magnetic properties of various nanoparticles with and without the metallic core	41

CHAPTER 1

INTRODUCTION

Nanoparticles (NP) have gained much interest in the field of biomedical applications because of the various ways that they can be tailored to suit different aspects of imaging, drug delivery etc. The common approach is to decorate the NPs with specific antibody so that they can be used to target different organs. An example is to coat the NPs with a sugar which are then taken up preferentially by tumors because of their higher metabolic rate. NPs with magnetic properties are very interesting because of the fact that they provide one with the capability of controlling them from outside via application of magnetic fields. In addition, they possess possible applications in various fields such as ultra-high-density magnetic recording, magnetic fluids and biomaterials. Magnetic nanoparticle (MNP) of biological interest because of their size ranges from a few nanometers to tens of nanometers which is comparable in size to cells (10-100micron), a virus (20-450nm), a protein (5-50nm) and a gene (2nm wide and 10-100nm long) [1]. Hence MNPs are extensively used in Magnetic Resonance Imaging (MRI). In MRI, an externally applied field is used to align the magnetization of atoms in the tissue. Once the field is turned off, the atoms revert back to their original spin state and the emitted field is detected. MNPs are used as agents to amplify this signal. MNPs can be used in as constituent in biocompatible ferrofluids which are used as drug delivery agent in tumor therapy. Such a method provides the advantage that the drug can be concentrated at a specific site and thus reduce the unwanted side effects in the organism. MNPs concentrated at such a site can be used for imaging purposes as well. Another usage of MNPs would be to use them as carrier for Positron emission tomography (PET) agents. Gamma rays emitted by such agents are regularly used for imaging purposes and hence one can easily visualize a scenario where the radioactive

species is encapsulated with a magnetic coating or vice versa and the resulting complex can be controlled from outside by applied magnetic field. MNPs are a class of NPs which can be manipulated by using external magnetic fields. MNPs are controlled by an external magnetic field which provides magnetic tagging of biomolecules, leading to efficient bioseparation, sensitive biosensing, MRI contrast enhancement and site-specific drug delivery. These NPs respond resonantly to alternating magnetic field which allows transfer of magnetic energy to the particle as form of heat and this can be used to destroy tumors. Many other potential applications can be made available for biomedical applications using several characteristics of NPs like size uniformity, surface area, adsorption kinetics, biocompatibility, superparamagnetism and magnetic moment which can be achieved during synthesis processes. A schematic of such MNP is shown in Figure 1.1 and is compared with other nanoparticle based complexes.

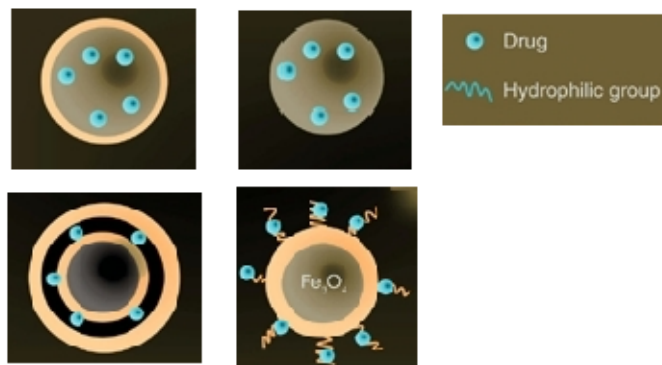


Figure 1.1 Schematic of nanoparticle drug complex represents a complex with magnetic core and decorated with drug and hydrophilic group

In vivo applications require particles to be biocompatible, stable and biodegradable. This can be achieved by coating or embedding particles with a suitable material. Carbon nanoparticles (CNP) are potentially biocompatible, chemically stable, and nontoxic can synthesize into various sizes and shapes. Hence it can be argued that carbon incorporated

MNPs will be well suited for biological applications. It has been shown that starch-coated magnetic iron oxide nanoparticles are tolerated quite well by living organisms [22, 23]. CNPs are made magnetic by incorporating ferromagnetic materials (Fe, Ni and Co) into it. These ferromagnetic metals are prone to environmental degradation and highly reactive due to high surface area. Incorporation with carbon protects metallic core from oxidation, agglomeration and opens the possibility of optimizing their intrinsic magnetic properties. Thus carbon incorporated MNPs can be used for biomedical applications. Various processes are employed to synthesize MNPs, including- dry processes such as arc discharge [1], [2], [3], [4] and [5], laser ablation [6], [7] and [8], chemical vapor deposition (CVD) [9], [10], [11], [12] and [13] and hydrocarbon flames [14]. Challenge in this field is to come up with a process which is cost effective and gives better control over the size distribution of the MNPs. This is the motivation for this thesis.

CHAPTER 2

BACKGROUND INFORMATION AND LITERATURE REVIEW

2.1 Introduction to magnetism

2.1.1 Basics of magnetism

The atomic nature of magnetism can be understood by considering the simple case of an electron orbiting around the nucleus. This picture can be compared to a current going around a loop. Based on Ampere's law, such a current carrying loop has a magnetic moment, μ , associated with it which is given by $\mu = Ia$, where I is the current in the loop with surface area S .

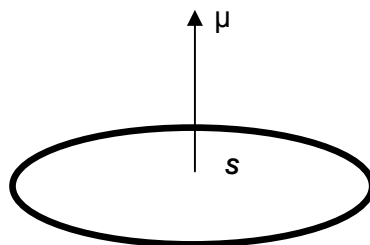


Figure 2.1 Illustration of a magnetic moment due to a current carrying loop.

The above classical picture combined with the spin of the electron gives rise to the net dipole moment associated with an atom having an unpaired electron. When a material is placed in an external magnetic field, all the dipoles respond to the field and this response is what distinguishes them into – paramagnetic, diamagnetic and ferromagnetic materials.

If a magnetic material is placed in a magnetic field of strength H , the individual atomic moments contribute to its overall response; the magnetic induction is given by:

$$B = \mu_0 (H + M)$$

Where, μ_0 is the permeability of free space, and the magnetization M is the magnetic moment per unit volume. The relation between M and H can be quite complicated (in case of ferromagnetic materials) linear (in case of diamagnetic and paramagnetic material).

2.1.2 Classes of Magnetic materials

As discussed above, the magnetic behavior of materials can be classified into the following three groups- Diamagnetism, paramagnetism and ferromagnetism.

Diamagnetism- It is a fundamental property of all matter and is usually very weak. Diamagnetic materials, which have no atomic magnetic moments, have no magnetization at zero field. When a field is applied a small negative moment is induced on the diamagnetic atoms proportional to the applied field strength.

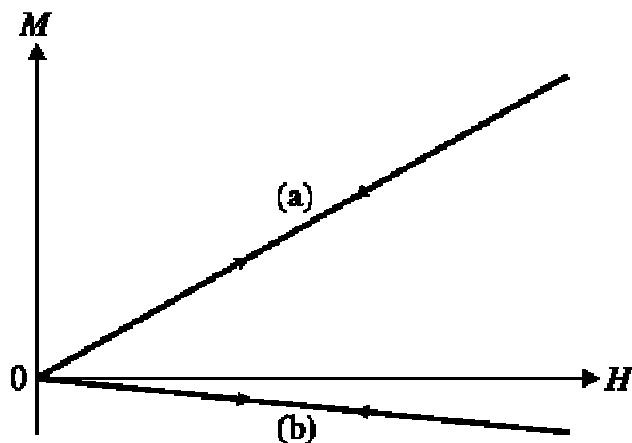


Figure 2.2 Effect on the magnetization (M) of an applied magnetic field (H) on (a) a paramagnetic system and (b) a diamagnetic system.

It can be seen that the slope of the straight line is negative. Writing the relationship between M and H , $M = \chi H$ where χ is the constant of proportionality and is called magnetic susceptibility. The Table 2.1 [15] shows magnetic susceptibility for some common materials. Notice that for diamagnetic materials, magnetic susceptibility is negative.

Table 2.1.Magnetic susceptibility of some common materials [15]

Material	Susceptibility	Material	Susceptibility
Diamagnetic		Paramagnetic	
Bismuth	-1.6x10-4	Oxygen	1.9x10-6
Gold	-3.4x10-5	Sodium	8.5x10-6
Silver	-2.4x10-5	Aluminum	2.1x10-5
Copper	-9.7x10-6	Tungsten	7.8x10-5
Water	-9.0x10-6	Platinum	2.8x10-4
Carbon dioxide	-1.2x10-8	Liquid Oxygen (-2000C)	3.9x10-3
Hydrogen	-2.2x10-9	Gadolinium	4.8x10-1

Paramagnetism - In paramagnetic materials, the atoms have a net magnetic moment but are oriented randomly throughout the sample due to thermal agitation, giving zero magnetization. As a field is applied the moments tend towards alignment along the field, giving a net magnetization which increases with applied field as the moments become more ordered (See Figure 2.1(a)). As the field is reduced the moments become disordered again by their thermal agitation.

Ferromagnetism- Unlike paramagnetic materials, the atomic moments in these materials exhibit very strong interactions. These interactions are produced by electronic exchange forces and result in a parallel or antiparallel alignment of atomic moments. Exchange forces are very

large, equivalent to a field on the order of 1000 Tesla, or approximately a 100 million times the strength of the earth's field. Ferromagnetic materials exhibit parallel alignment of moments resulting in large net magnetization even in the absence of a magnetic field. The elements Fe, Ni, and Co and many of their alloys are typical ferromagnetic materials. The two distinct characteristics of ferromagnetic materials are- Spontaneous magnetization and the existence of magnetic ordering temperature.

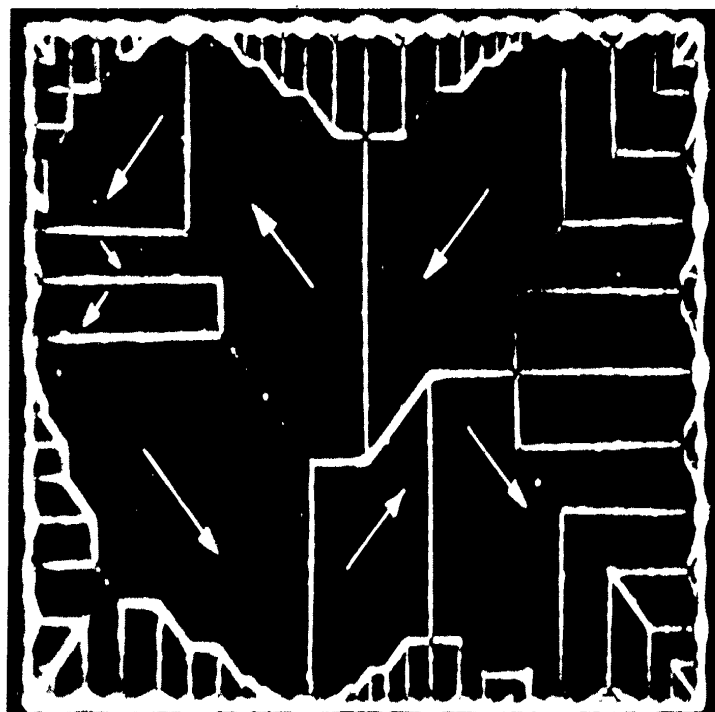


Figure 2.3 Microscopic view of the domains in a ferromagnetic material [15]

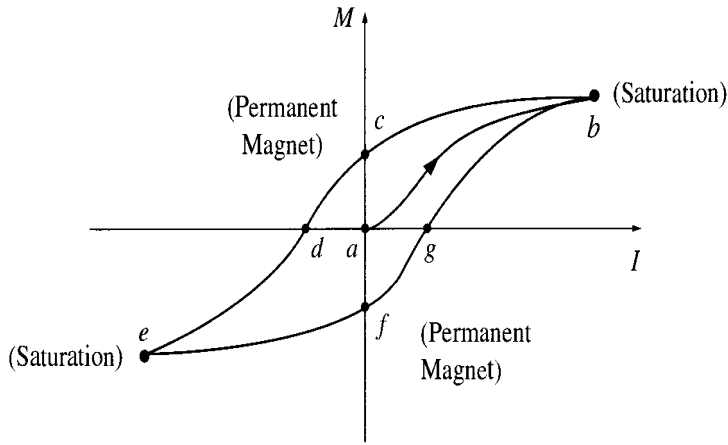


Figure 2.4 Magnetization behavior of a ferromagnet with an applied field

The effect of the applied field is such that the domains (Figure 2.3) with favorable magnetic dipole will grow at the expense of the other ones since energetically the former are favorable. When the external field is switched off, the domains do not revert back to their original orientation and this is the origin of permanent magnet.

2.1.3 Various energy terms

Magnetic phenomena in small magnetic structures can be understood by considering that the state of magnetization is determined by minimizing the combination of 4 energy terms: Zeeman energy, Exchange energy, Magnetocrystalline energy and Magnetostatic energy.

Zeeman energy- This refers to the energy of magnetization in an externally applied magnetic field. It is often referred to as magnetic potential energy. Zeeman energy is always minimized when the magnetization is aligned with the external magnetic field. Zeeman energy is expressed as:

$$E_z = \vec{M} \cdot \vec{H}$$

Where, 'H' is the magnetic field applied and M is the moment.

Exchange energy - It is a measure of the strength of the electrons spin exchange coupling. This energy term is responsible for the metals like iron, Cobalt and Nickel to be ferromagnetic. Exchange energy is lowest when atomic moments align themselves parallel to each other.

Magnetocrystalline anisotropy- Not only the atomic moments point to one direction but they point to a particular crystallographic orientation which is called easy axis. Anisotropy energy is the energy required to change the direction of atomic moments from easy axis to hard axis. Anisotropy energy is defined as:

$$E=K\sin^2\Theta$$

Where, K is the anisotropy constant and θ is the angle between direction of magnetization and the principal axes of the crystal.

Magnetostatic energy - A uniformly magnetized specimen has a large magnetostatic energy which is the result of presence of magnetic free poles at the surface of the specimen. These free poles generate a demagnetizing field. The high energetic cost of forming magnetostatic charges on the surface can often be reduced by introducing non-uniform magnetizations. This may increase the exchange energy, crystalline anisotropy energy and Zeeman energy, but the total energy is lowered. This sometimes results in the formation of a structure within magnetic elements called domains.

2.1.4 Effect of particle size on magnetic property

Magnetic property of materials such as coercivity, and remanence vary greatly with the particle size. Based on their sizes these magnetic materials are divided into three categories i.e. single domain, multidomain and superparamagnetic.

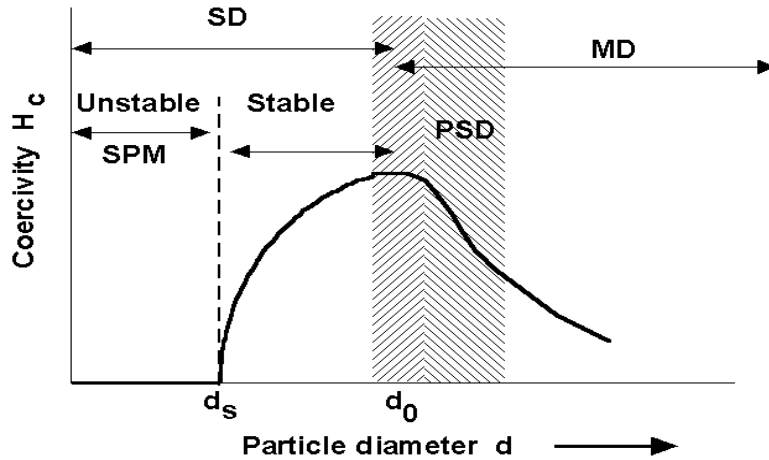
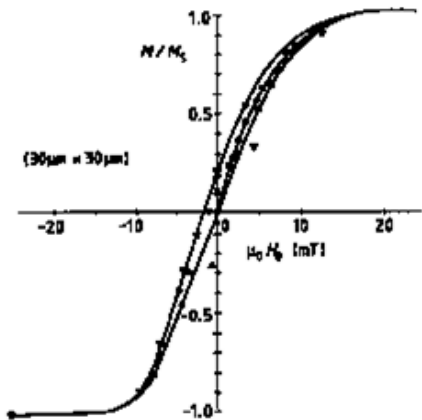


Figure 2.5 Change in hysteresis loop with change in particle size for single domain particle, multi domain particle and superparamagnetic particle.

Single domain and multi domain states

A single domain is uniformly magnetized with saturation magnetization (M_s) along the easy axis, thus minimizing exchange and anisotropy energies. The magnetostatic energy can be reduced if the grain divides into two domains each magnetized with M_s in opposite direction, thus reducing remnant moment of the grain, an energetically difficult process. Thus, single domain grains are magnetically hard and have high coercivity and remanence. Hysteresis curve for single domain particle is shown in 2.6 (b). Multidomain grain is not uniformly magnetized. Inside each domain the magnetization $M_i=M_s$, but the direction of M_i varies between different domains resulting in the grain as a whole having net remanence $M_i \ll M_s$. so as the grain size increases number of domains also increases. As shown in Figure 2.5 for multidomain as the particle size increase coercivity decreases whereas for single domain grains as size increase coercivity increases.

MD type



SD type

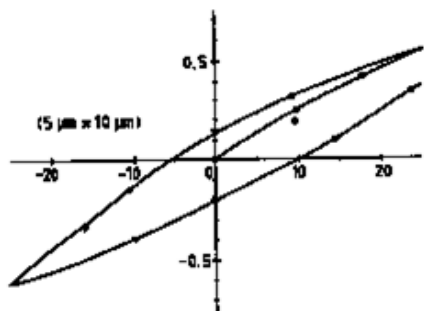


Figure 2.6 Hysteresis loop for multidomain (MD) and single domain (SD)

Superparamagnetism

As particle size continues to decrease within the single domain range critical threshold is reached at which remanence and coercivity go to zero the grain becomes superparamagnetic (SPM). A single domain particle of volume v has a uniform magnetization directed along the easy axis of magnetization. If v is small enough, or the temperature is high enough, thermal energy (kT) will be sufficient to overcome the anisotropy energy separating the (+) and (-) magnetization states and cause a spontaneous reversal of magnetization. For superparamagnetic particles, the net magnetic moment in zero field and at $T > 0K$, will average to zero. In an applied field, there will be a net statistical alignment of magnetic moments. This is analogous to paramagnetism, except now the magnetic moment is not that of a single atom, but to a single domain particle. Hence, the term superparamagnetism, which denotes a much higher susceptibility value than that for simple paramagnetism. In response to a change in the applied field or temperature, an ensemble of SPM particles will approach an equilibrium value of magnetization with a characteristic relaxation time given by

$$\frac{1}{t} = f_0 \exp\left(-\frac{KV}{kT}\right)$$

Where, f_0 is frequency factor (10^9 sec^{-1}), K is anisotropy constant, V is particle volume, k is Boltzmann constant and T is the absolute temperature. The exponential nature of the relaxation time on V and T makes it possible to define a blocking temperature, T_B (at constant volume), or blocking volume V_B , (at constant temperature) at which the magnetization goes from an unstable condition ($t \ll t_r$) to a stable condition ($t > t_r$). At a certain temperature (blocking temperature) the measurement time equals relaxation time and the grains become superparamagnetic and carry no remanence. Grains that are SPM at room temperature can become blocked and SD at low temperatures. The relaxation behavior of superparamagnetic grains as a function of temperature is used to detect presence of grains in biological samples by measuring the temperature dependence of magnetic remanence. SPM grains show extremely thin hysteresis loop as they exhibit zero coercivity as shown in Figure 2.7.

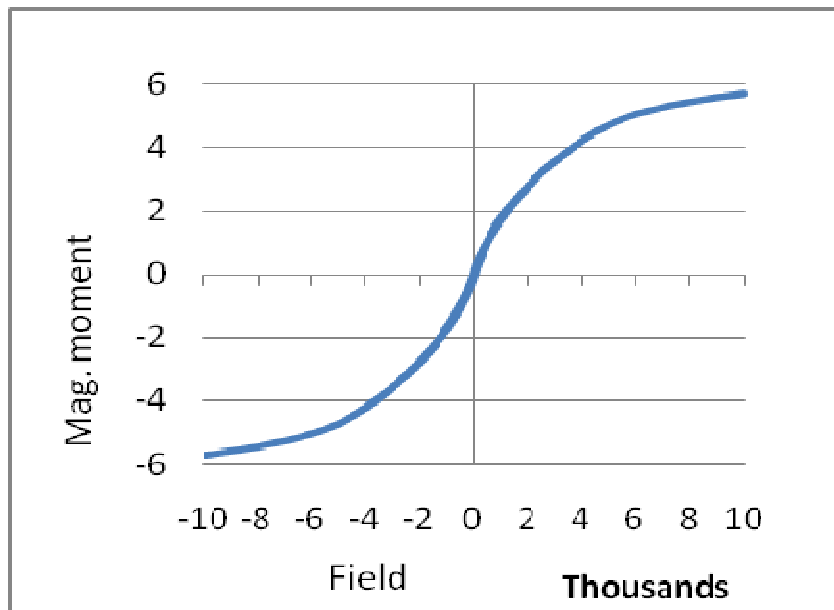


Figure 2.7 Hysteresis curve of superparamagnetic particles

2.2 Literature review on synthesis of carbon magnetic nanoparticles

Carbon incorporated NPs have been synthesized by a conventional arc discharge method in a helium atmosphere. To synthesize the carbon nanoparticles (CNP) by this method, a pure graphite cathode and a composite carbon rod anode (containing metal or metal oxide precursors) undergo arc-vaporization. Major problem with this method is the production of large amounts of unwanted carbonaceous debris (graphite flakes, carbon nanotubes, amorphous carbon) and micron-sized metallic particles which makes the application of the graphite-encapsulated NPs difficult. This problem was corrected by tungsten arc technique, which lowered the amount of carbonaceous debris produced by decreasing the carbon content of the arc in a helium atmosphere. The resultant product contained un-bonded metal NPs, incorporated metal NPs and only a small amount of amorphous carbonaceous debris. Both conventional and the modified arc discharge method requires expensive vacuum equipment, and the power required usually exceeds 1 kW. On the other hand, an arc discharge in liquid media needs no vacuum system, but it does require a high electric power input for the generation of the discharge. The arc discharge in gas and liquid media is initiated by contacting an anode with the cathode; without this initiation a high transient breakdown voltage is necessary to generate the plasma discharge in a neutral medium. For example, electric breakdown voltages of liquid hydrocarbons are quite high, around several tens of kilovolts, with an electrode separation of 0.5–8 mm.

New synthesis method for producing iron NPs wrapped in multilayered graphitic shells is described below. This method takes advantage of the fact that electric plasma can be generated and maintained in an organic liquid under ultrasonic irradiation. Ultrasonic cavitation causes a very highly localized high temperature and pressure (>5000 K, > 100 MPa) region

where tiny bubbles are collapsing – a region referred to as a “hot spot”. An ultrasonic cavitation field, with its many activated tiny bubbles, may enhance electrical conductivity due to the high-energy species (radicals, atoms, ions and free electrons) formed within it. Thus, an electric plasma discharge could be generated at a remarkably low voltage such as 55 V DC. Without the ultrasonication, no plasma discharge could take place at such a low level of electric power. The organic liquid and metal electrodes act as precursors for the synthesis of the graphite shell encapsulating metal core. This new synthesis method does not require a vacuum system because the plasma discharge occurs in a liquid at atmospheric pressure. In addition, the liquid provides high speed quenching which may assist in the formation of uniform.

CHAPTER 3

SYNTHESIS AND CHARACTERIZATION METHODS

3.1 Experimental setup

Of the various ways to synthesize CNPs, ultrasonic cavitation is the most versatile as it provides one with large number of parameters to play with- frequency, liquid medium, material for the ultrasonic horn etc. The most important property of the ultrasonic method is that one can achieve very short duration of high temperature (~500K) and pressure which cannot be so readily achieved by other processes [16].

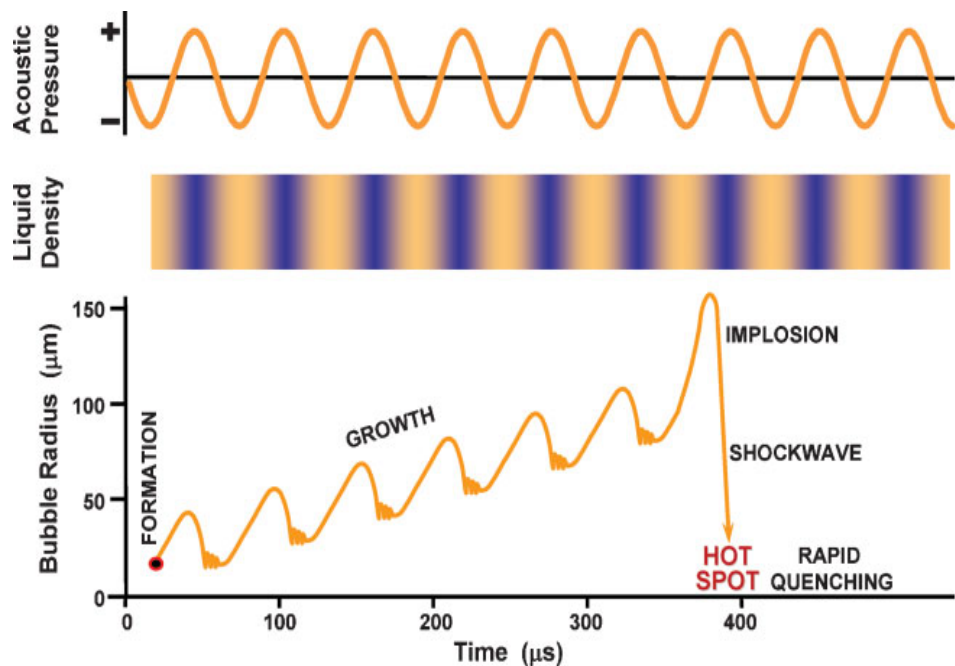


Figure 3.1 Schematics of acoustic pressure, liquid density and the bubble formation followed by ultrasonic cavitation [16].

Figure 3.1 demonstrate the basic mechanism of the NPs formation by ultrasonic method. When the liquid is subjected to ultrasound, the alternating expanding and contracting forces

create bubbles and makes them oscillate. The bubbles grow up to micrometer in size before collapsing and thus releasing the energy stored in them in a very short period. This results in a heating rate of $\sim 10^{10}$ K/s. This thermal energy produces radicals and free electrons in the “hot spot” region by bond cleavage and rearrangements [16]. If such a hot spot can be created between two electrodes which are placed close to each other (~mm apart), then a plasma discharge can be achieved between the two electrodes [16, 17]. This is because of the enhanced conductivity due to the presence of the hot spot. The discharge incorporates some of the metal electrode material into the formed NPs.

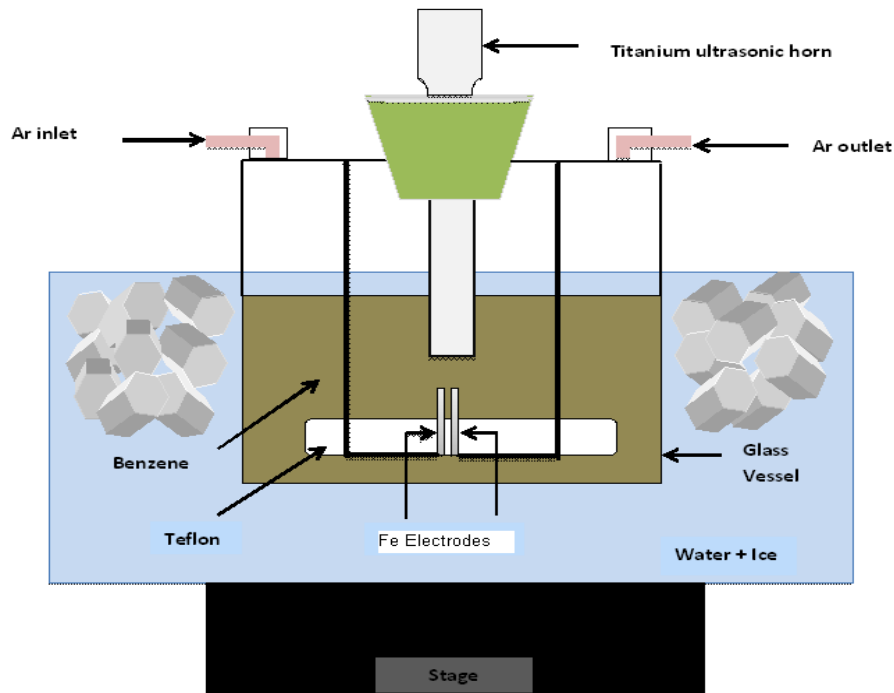


Figure 3.2 Schematic diagram of experimental setup

The schematic diagram of the experimental setup is shown in Figure 3.2. It consists of a glass vessel fitted with a titanium ultrasonic horn. Two iron electrodes (purity 99.7%) are placed

less than 1mm apart from each other just beneath the ultrasonic horn. The ultrasonic horn was used at 600W and 20 kHz in the experiments to irradiate 100 ml of liquid benzene. During the experiment, a constant flow of Argon gas was maintained to keep a neutral environment. During the irradiation, the voltage on the electrodes was kept at 3.7 kV and 4.1kV DC using a constant voltage power unit. The upper limit of the current of the unit was set at 1.58 mA. Electric plasma was generated in the cavitation field just beneath the horn. The current on the electrodes became momentarily higher than the current limit of power unit when the plasma discharge occurred. The plasma flashes due to the intermittent decrease of the voltage when the current exceeded the limit of the power unit. However, without ultrasonic irradiation, no plasma was generated using the present electric power supply. During the experiment, small amount of electrodes are consumed by thermal evaporation. After 1 hour, the black powder produced was separated by centrifugation from the benzene and dispersed in ethanol. It was dried in a vacuum oven at 313 K to get the CNP agglomerate. CNPs were synthesized at different parameters i.e. at different voltage and different electrodes. One set of CNPs were prepared at a voltage of 3.7 kV and other set at voltage 4.1 kV using iron electrodes. One set of CNPs were prepared at voltage 4.1 kV using graphite electrodes.

3.2 Magnetic characterization

3.2.1 Magnetic Property Measurement System Superconducting Quantum Interference Device (MPMS-SQUID)

The magnetic characterizations were carried out using a Quantum Design Magnetic property Measurement system (MPMS) XL SQUID magnetometer (SQUID= Superconducting Quantum Interference Device). It makes very accurate and sensitive measurements of the magnetic moment. SQUID works on the principle of - superconductivity, Josephson tunneling through a weak link and flux quantization into a superconducting ring. Superconductivity is

observed in certain materials when they are cooled below a certain temperature called T_c (critical temperature). Below T_c , the materials become perfect conductors. The Josephson junction is composed of two superconductors separated by a thin insulating layer. This insulating layer is referred to as the weak link [19].

Next, I describe the RF-SQUID which is used in the MPMS-Quantum Design magnetometer. The superconducting current in a single junction ring placed in a magnetic field can be shown to have the form [20, 21]

$$I_s = I_C \left[\sin 2\pi \left(1 - \frac{\phi_i}{\phi_0} \right) \right]$$

Where, I_C is the critical current, ϕ_0 is a flux quantum and ϕ_i is the incident flux on the ring. The incident flux on the ring, ϕ_2 is the sum of the external applied flux to be measured ϕ_x , and the flux from the coupling to the resonant circuit formed by the ring.

The main parts of the MPMS are the SQUID, the magnetometer, the probe assembly, the Dewar and the electronic control system. Since the superconducting materials will screen out any field and fact that SQUID must be operated within a magnetic shield leads one to obtain the measurements by linking the SQUID through a flux transformer to a detecting magnetometer. This setup has been shown schematically in Figure 3.3

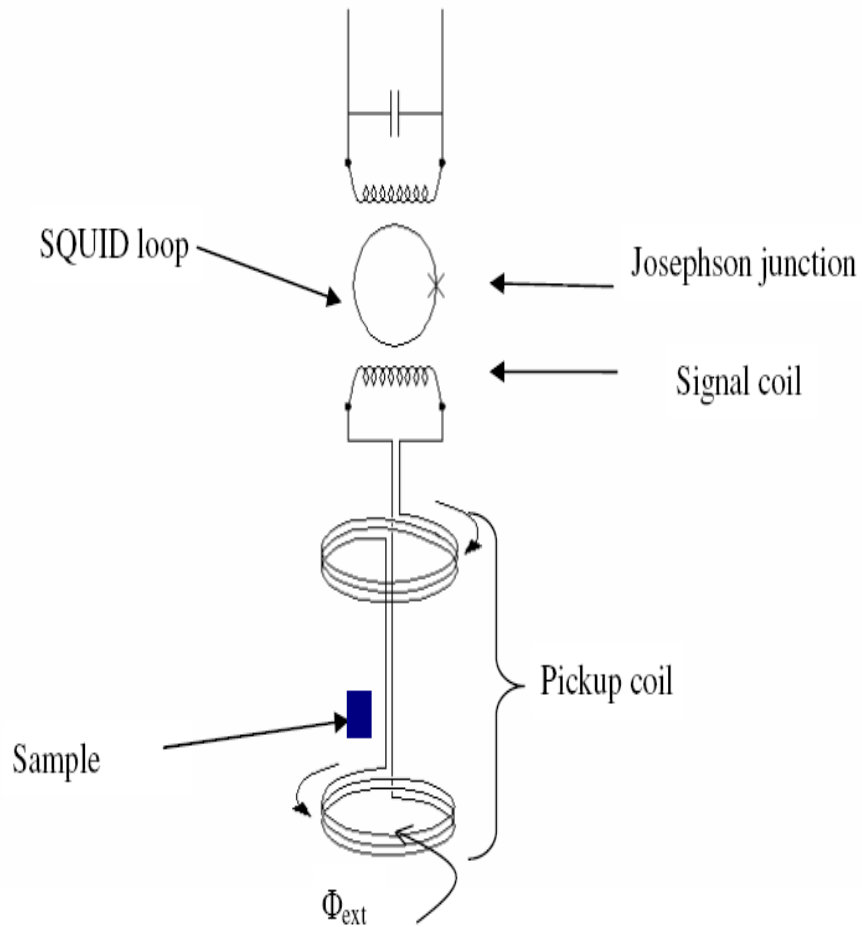


Figure 3.3 Setup for MPMS SQUID magnetometer

The range of measurements for MPMS is 10^{-8} emu to 2 emu. The sample is placed in a uniform magnetic field and moved slowly in a 3 cm length through a set of superconducting detection coils. Using a second order gradiometer coil arrangement, the detecting system is insensitive to the uniform field applied. Thus, only the magnetic moment of the sample induces the electric current in the detection coils. The entire setup is maintained in the range of 4.2 K to 400k by using liquid Helium

3.3 Microstructure characterization

3.3.1 Transmission electron microscope (TEM)

Figure 3.4 shows the TEM machine. The microscope images the crystal lattice of a material as an interference pattern between the transmitted and diffracted beams. This allows one to observe planar and line defects, grain boundaries, interfaces, etc. with atomic scale resolution. The bright field and dark field imaging modes of the microscope, which operate at intermediate magnification, combined with electron diffraction, are also invaluable for giving information about the morphology, crystal phases, and defects in a material



Figure 3.4 Transmission electron microscope (model no. H-9500)

In TEM sample preparation, small amount of dried powder is suspended in water and then dropped onto a copper micro grid covered with carbon film. In preparation for the 300 kV HRTEM (H-9500) investigations the grid is allowed to dry and then inserted into the HRTEM. The TEM observations allowed us to determine the overall morphology of the specimen and the structures of the CNP's. Some of the observed nanoparticles were examined by means of

selected area electron diffraction (SAED). To identify the elemental composition of the CNP's we carried out energy dispersive X-ray (EDX) studies. During EDX, NPs are bombarded with electron beam inside the electron microscope. The bombarding electrons collide with the atoms of the specimen and knocking some of the core electrons in the process. A hole is created in the inner shell electron shell which is eventually occupied by a higher-energy electron from outer shell. The extra energy in the system is released in the form of X-ray. Amount of energy released depends on factors like from which shell electron is transferring from as well as to which shell it is transferring to. Atoms of every element releases X-rays with exclusive amount of energy during the electron transferring process. Thus, the X-ray photon's energy serves as a signature for specific elements. EDX spectrum displays peaks corresponding to the energy levels for which the X-rays have been received. Each peak is unique to an atom and hence corresponds to a single element. The peak intensity is directly proportional to the concentration of the element is in the specimen.

3.4 Raman spectroscopy

The Raman Effect occurs when light impinges upon a molecule and interacts with the electron cloud and the bonds of that molecule. For the spontaneous Raman Effect, a photon excites the molecule from the ground state to a virtual energy state. When the molecule relaxes it emits a photon and it returns to a different rotational or vibrational state. The difference in energy between the original state and this new state leads to a shift in the emitted photon's frequency away from the excitation wavelength. If the final vibrational state of the molecule is more energetic than the initial state, then the emitted photon will be shifted to a lower frequency in order for the total energy of the system to remain balanced. This shift in frequency is designated as a Stokes shift. If the final vibrational state is less energetic than the initial state, then the emitted photon will be shifted to a higher frequency, and this is designated

as an Anti-Stokes shift. Raman scattering is an example of inelastic scattering because of the energy transfer between the photons and the molecules during their interaction. A change in the molecular polarization potential or amount of deformation of the electron cloud with respect to the vibrational coordinate is required for a molecule to exhibit a Raman Effect. The amount of the polarizability change will determine the Raman scattering intensity. The pattern of shifted frequencies is determined by the rotational and vibrational states of the sample.

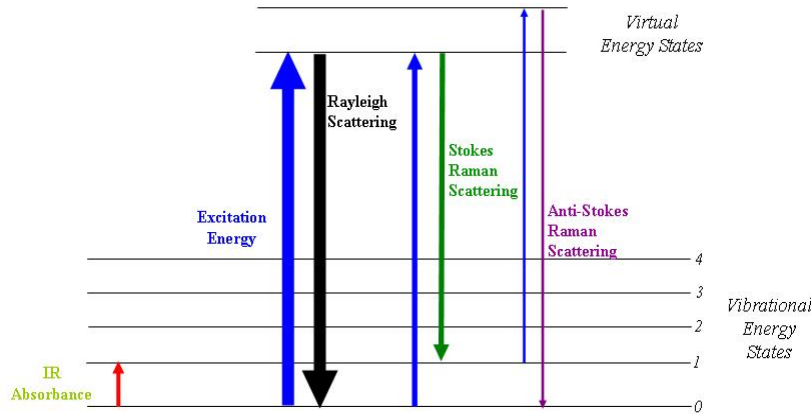


Figure 3.5 Schematics of Raman process.

3.5 X-ray Photoelectron spectroscopy (XPS)

For each and every element, there will be a characteristic binding energy associated with each core atomic orbital i.e. each element will give rise to a characteristic set of peaks in the photoelectron spectrum at kinetic energies determined by the photon energy and the respective binding energies. These characteristic peaks correspond to the electron configuration of the electrons within the atoms, e.g., 1s, 2s, 2p, 3s, etc. The number of detected electrons in each of the characteristic peaks is directly related to the amount of element within the area (volume) irradiated. To generate atomic percentage values, each raw XPS signal must be corrected by dividing its signal intensity (number of electrons detected) by a "relative sensitivity factor" (RSF)

and normalized over all of the elements detected. Figure 3.6 shows basic schematic diagram of XPS.

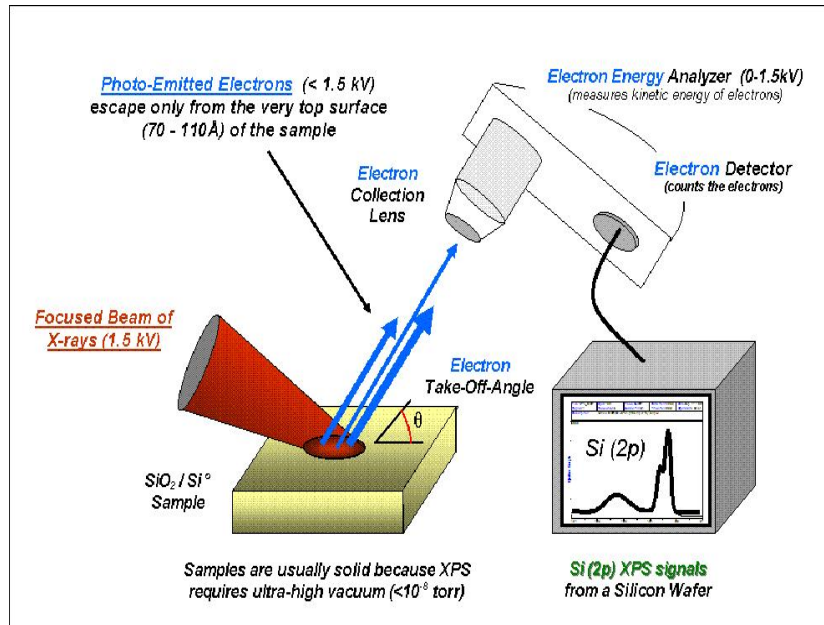


Figure 3.6 Schematic of X-ray Photoelectron Spectroscopy depicting the incident X-ray and the emitted photoelectrons

The energetic of the XPS process is given by the following relationship

$$K.E = h\nu - B.E - \varphi^-$$

Where, K.E is the kinetic energy of the emitted photoelectron, $h\nu$ is the energy of incoming photon beam, B.E is the binding energy of the emitted electron and φ^- is the electron workfunction.

CHAPTER 4

RESULTS AND DISCUSSIONS

Three different types of NPs were synthesized- (a) using iron electrodes at voltage 3.7kV (b) using iron electrodes at voltage 4.1kV and (c) using graphite electrodes at voltage 4.1kV. In the following sections, the magnetic, elemental and structural properties of these three samples are discussed.

4.1 Fe-CNP synthesized at 3.7 kV using iron electrodes

Iron doped CNPs (Fe-CNPs) were synthesized using voltage of 3.7 kV between the electrodes as shown in Figure 3.2. The distance between the iron electrodes was maintained at 0.5 mm. The magnetic properties were studied using SQUID magnetometer. Hysteresis loop of the iron incorporated CNPs are shown in Figure 4.1. It can be deduced that the Fe-CNPs are superparamagnetic as they have zero coercivity.

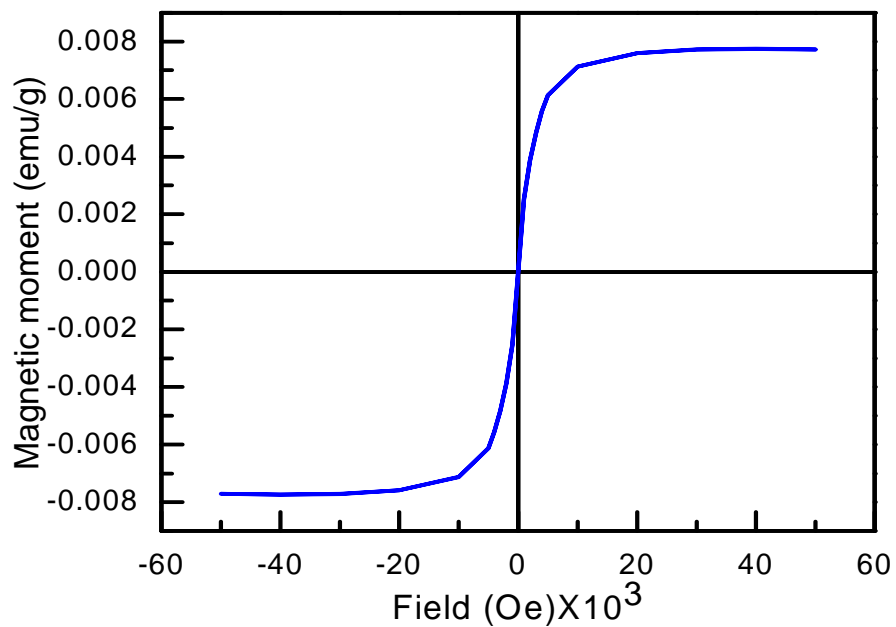


Figure 4.1 Hysteresis curve for sample produced with iron electrode at 3.7 KV

The structures of the CNPs were determined by High resolution Transmission Electron Microscopy (HRTEM). The images of the Fe-CNP are shown in Figure 4.2. The iron core can be observed as producing the diffraction fringe in the image. The metal cores tend to have random shape with the size in the range of ~ 10 nm.

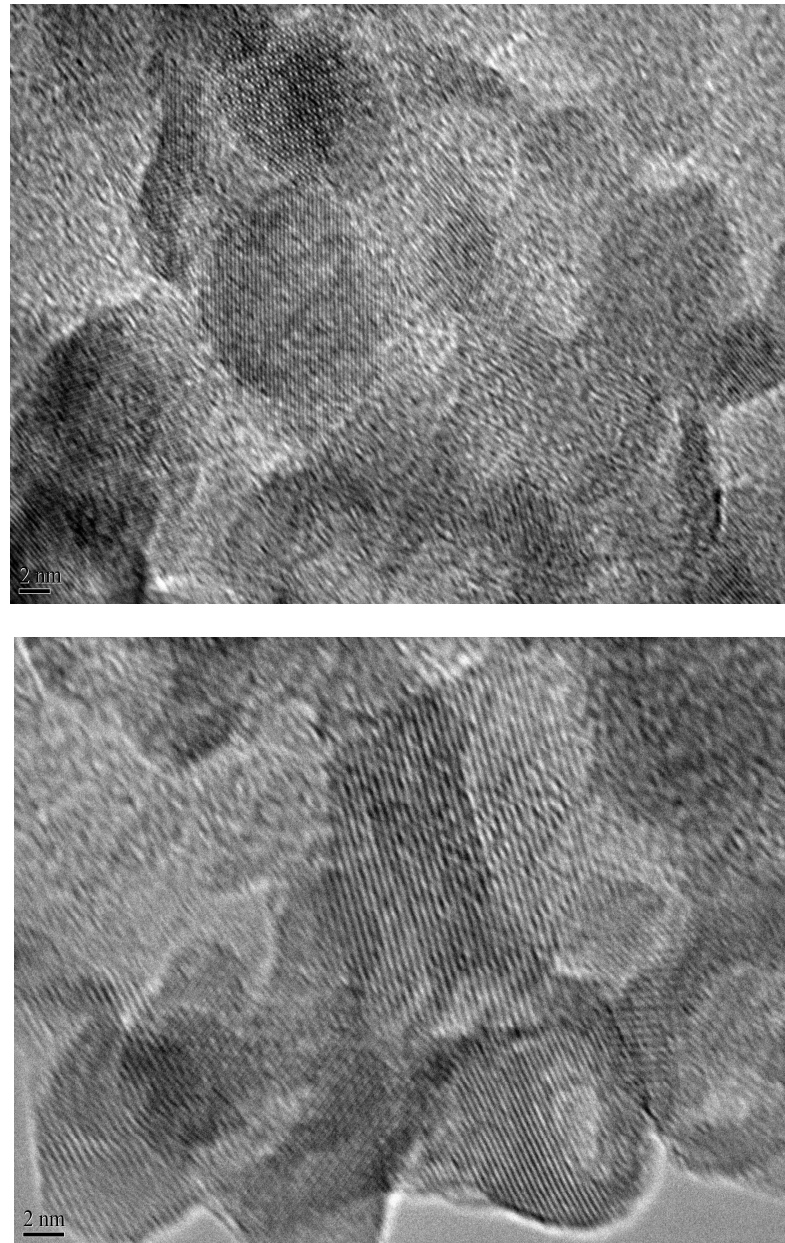


Figure 4.2 HRTEM image of Fe-CNPs synthesized at 3.7 kV using iron electrodes

The structure of the carbon phase of the Fe-CNPs was further analyzed by Raman Spectroscopy using two different wavelengths. The results are shown in Figure 4.3. Two

prominent peaks are seen at \sim 1355 and \sim 1590 cm^{-1} . Following the convention, they are labeled D and G peaks respectively.

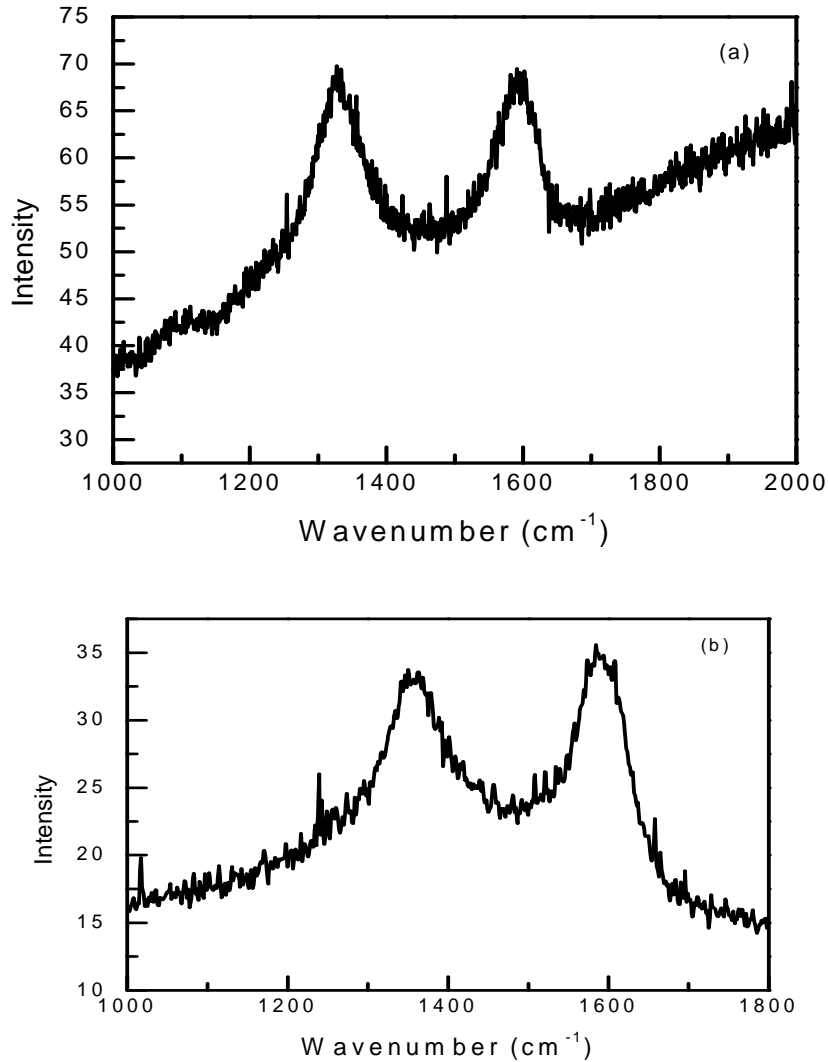


Figure 4.3 Raman spectrum of carbon nanoparticles synthesized at 3.7 kV using iron electrodes

4.2 Fe-CNP synthesized at 4.1 kV using iron electrodes

Fe-CNPs were synthesized at 4.1 kV using iron electrodes to test the effect of voltage on the magnetic and structural properties of the nanoparticles. The hysteresis curve for the powder

sample is shown in Figure 4.4. The Fe-CNPs are clearly superparamagnetic. Thus one can incorporate the magnetic particles in carbon shell leading to novel magnetic properties.

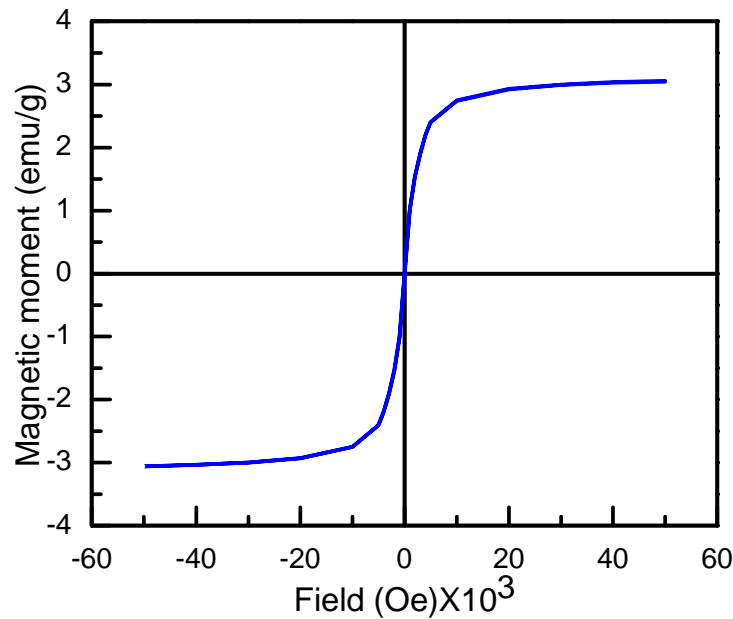


Figure 4.4 Hysteresis curve for Fe-CNP produced with iron electrode at 4.1 kV

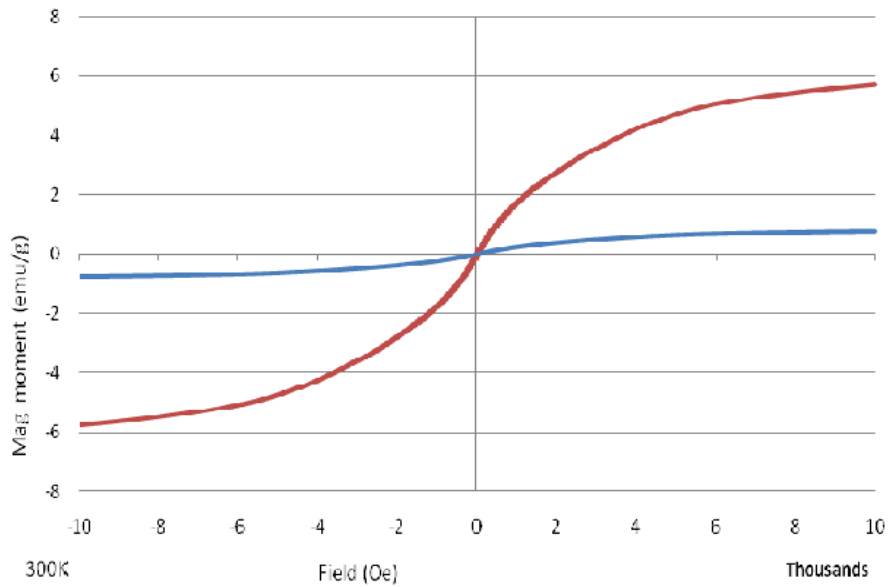


Figure 4.5 Comparison of Fe-CNP produced at 3.7 kV and 4.1 kV.

On comparison, it was found that the Fe-CNPs synthesized using iron electrodes at high voltage have saturation magnetization is six times that of when using lower voltage.

The elemental characterization of Fe-CNPs was carried out using EDX. As can be seen from Figure 4.6 and Table 4.2, Carbon constitutes ~95% of atoms in the Fe-CNP. The sample holder is made up of copper so there is peak at 8keV for Cu. The HRTEM images of Fe-CNP are shown in Figure 4.6 and Figure 4.7.

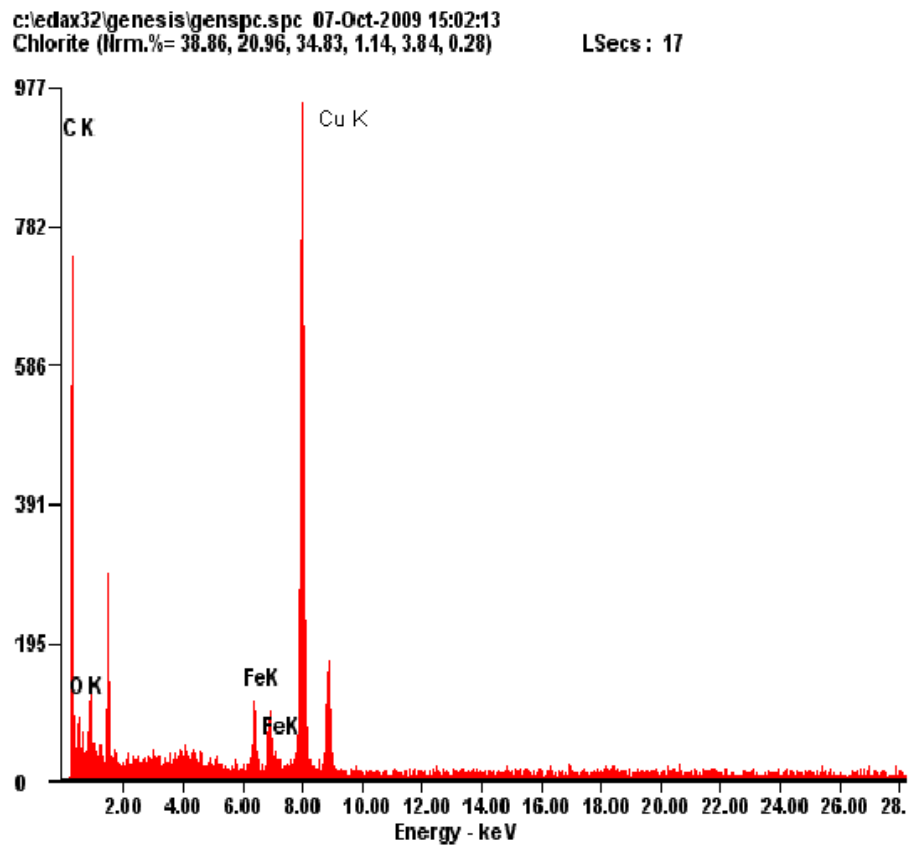


Figure 4.6 Elemental characterizations of Fe-CNP synthesized using iron electrodes and at 4.1kV.

Table 4.1 Summary of the Energy dispersive X-ray analysis as shown in Figure 4.6

Element	Weight %	Atomic%
C	87.80	94.60
O	04.50	03.60
Fe	7.80	1.80

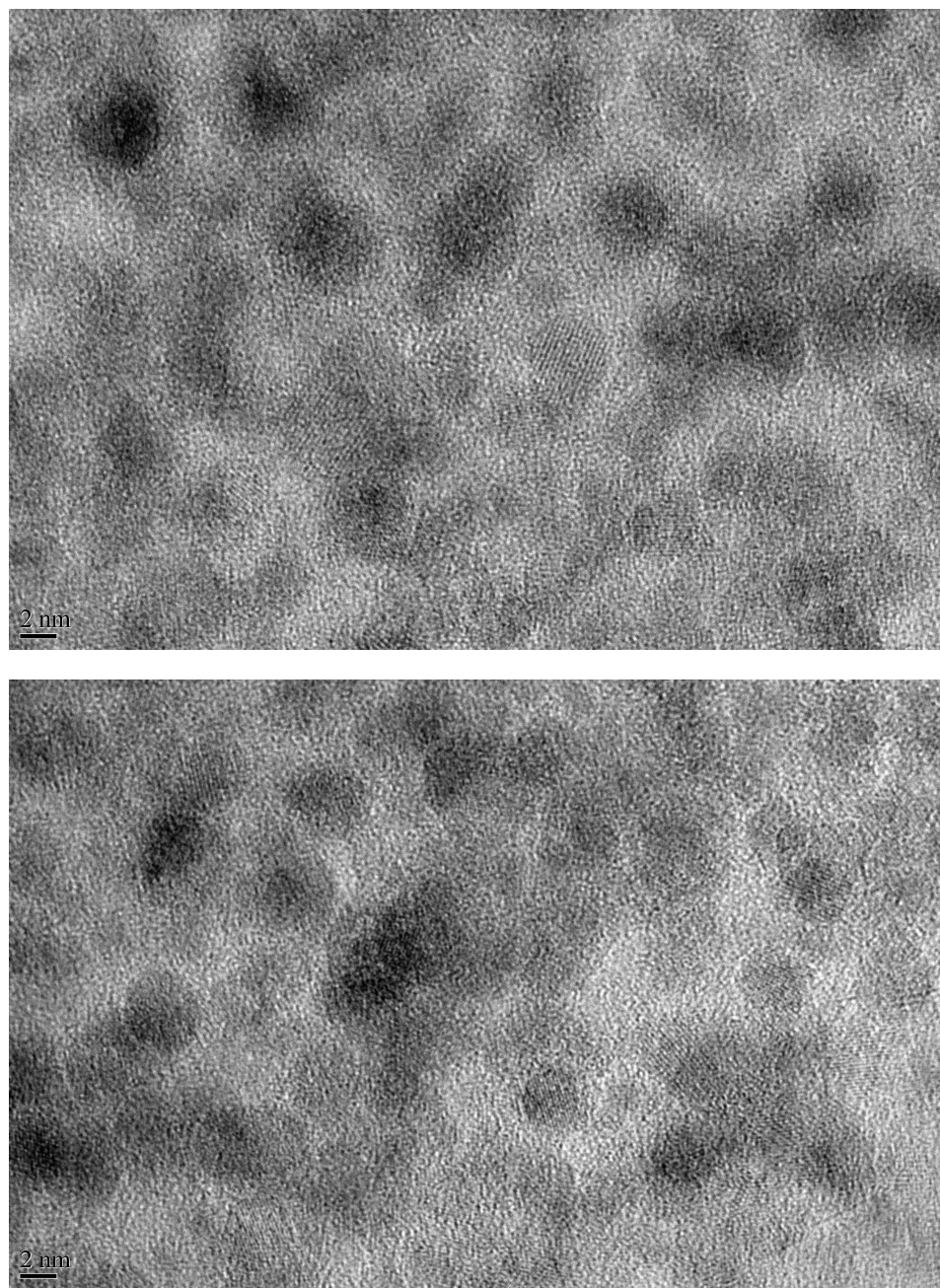


Figure 4.7 HRTEM image of Fe-CNP synthesized at 4.1kV using iron electrodes

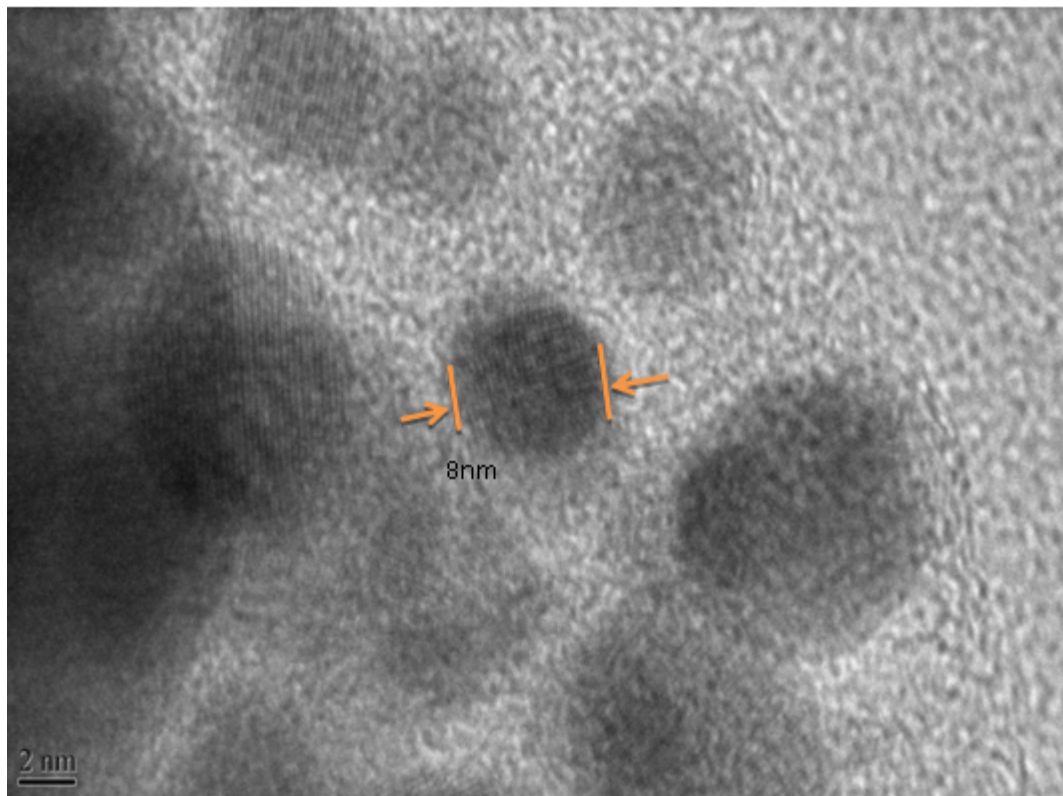


Figure 4.8 HRTEM image of Fe-CNP synthesized at 4.1 kV

As can be seen from the HRTEM images the average particle size of the CNP's are ~10nm. The core of the Fe-CNP shows diffraction fringes which point to the crystalline structure. The carbon phase forms an onion shell like structure around the crystalline phase.

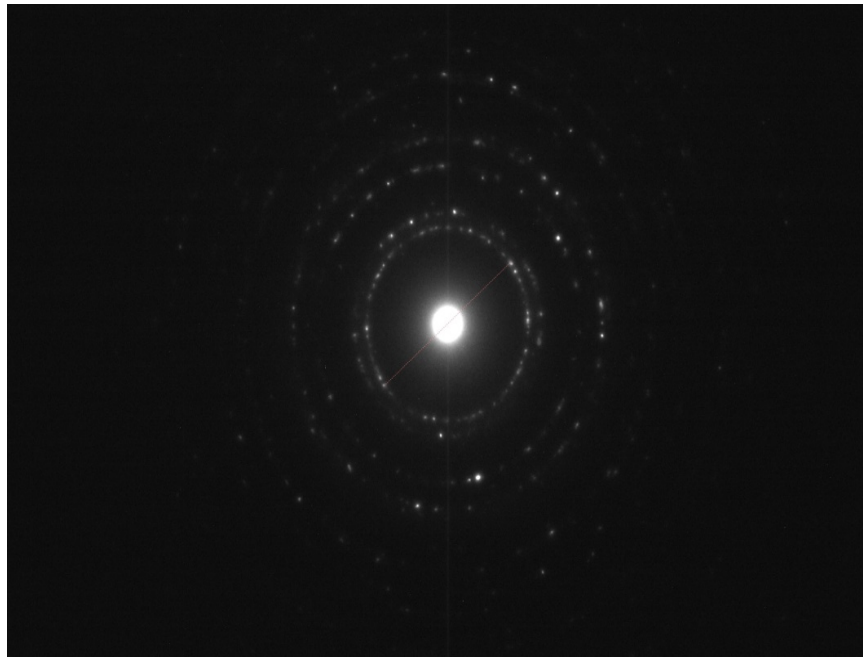


Figure 4.9 Selected area diffraction pattern of Fe-CNP synthesized at 4.1 kV

Table 4.2 d-spacing as calculated from Figure 4.9

	d1	d2	d3	d4
Interplanar spacing	0.228nm	0.196nm	0.139nm	0.118nm

The Raman spectra of the Fe-CNP are shown in Figure 4.10. The D and the G peaks for 633nm laser (Figure 4.10(b)) are at 1334 cm^{-1} and 1584 cm^{-1} . Compared to the Fe-CNP synthesized at 3.7 kV, the G peak, in this case, is extremely reduced. In fact, the Raman spectrum resembles that of diamond which has a single sharp peak at 1331 cm^{-1} [18]. Thus there is some indication that the Fe-CNP, synthesized at 4.1 kV, are diamond –like.

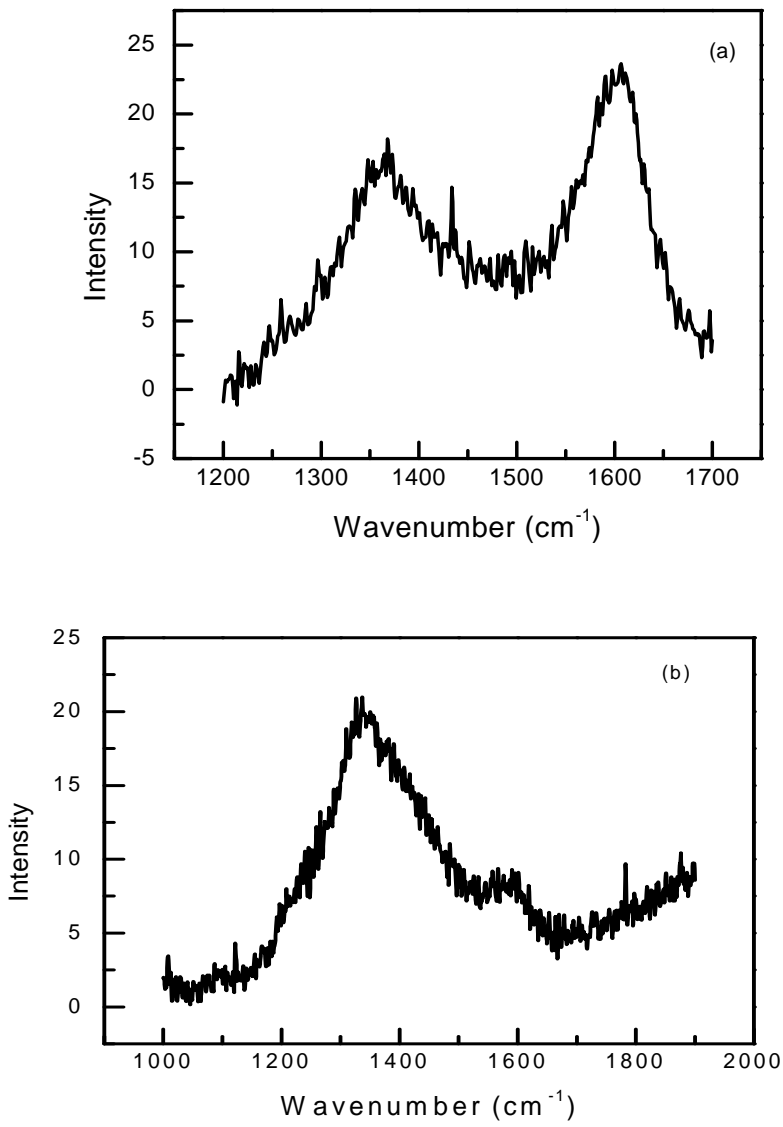


Figure 4.10 Raman spectroscopy using (a) blue and (b) red Laser of Fe-CNP synthesized at 4.1kV.

The slightly crystalline nature of the Fe-CNP is confirmed by the X-ray diffraction spectrum shown in Figure 4.11. A small peak is visible at $\sim 42^\circ$. This corresponds to the Fe-[111] plane or Fe_3C – [103] plane or a combination of both [22].

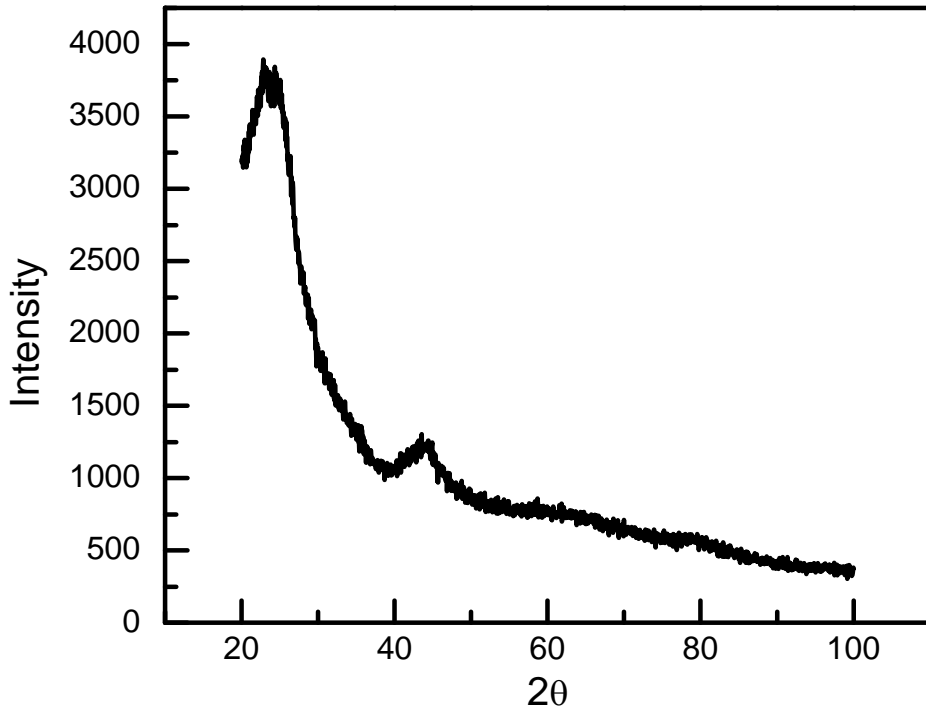


Figure 4.11 X-ray diffraction of carbon nanoparticles synthesized with iron electrodes at 4.1kV

4.3 CNP synthesized at 4.1 kV using graphite electrodes

The magnetic properties of the CNP synthesized using graphite electrodes were measured with the help of SQUID magnetometer using an applied field ranging from -10K to 10k Oe. Hysteresis curves of powder samples prepared at voltage 4.1kV using graphite electrode showed that it is ferromagnetic. It is having a ratio of remanent to saturation magnetization, $M_r/M_s=15\%$ at room temperature. The coercivity (H_c) was 200 Oe and saturation magnetization is 0.065emu/g at applied field of 10000Oe as shown in Figure 4.12.

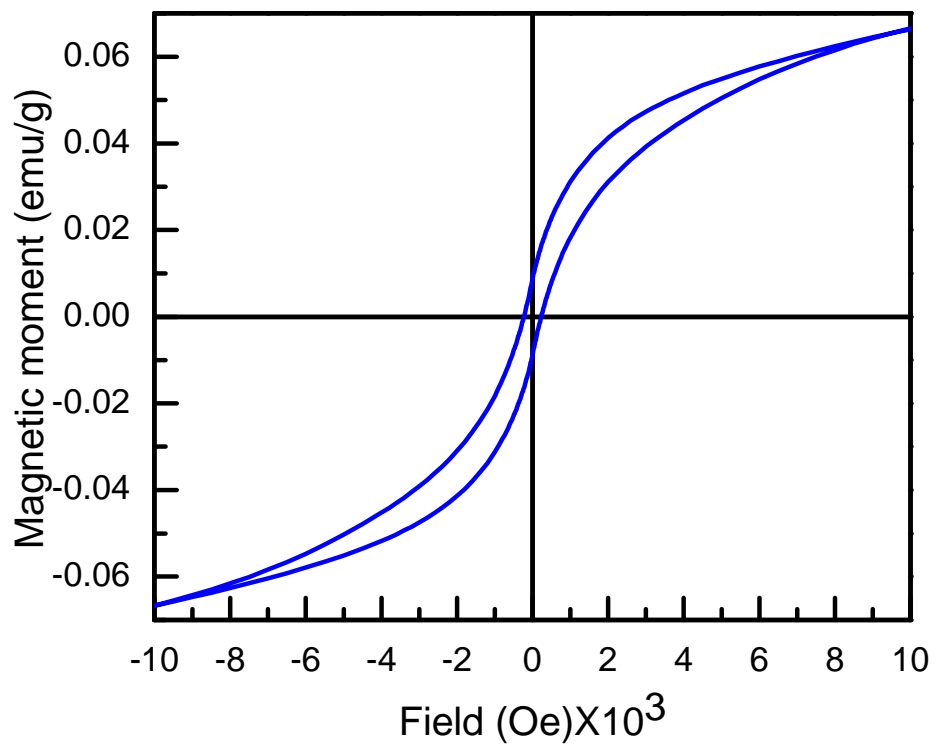


Figure 4.12 Hysteresis curve for CNP produced with graphite electrode at 4.1kV.

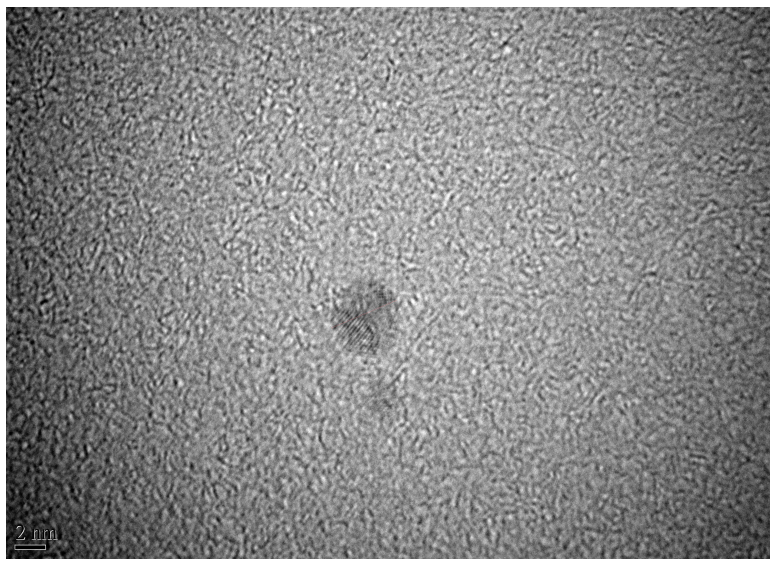
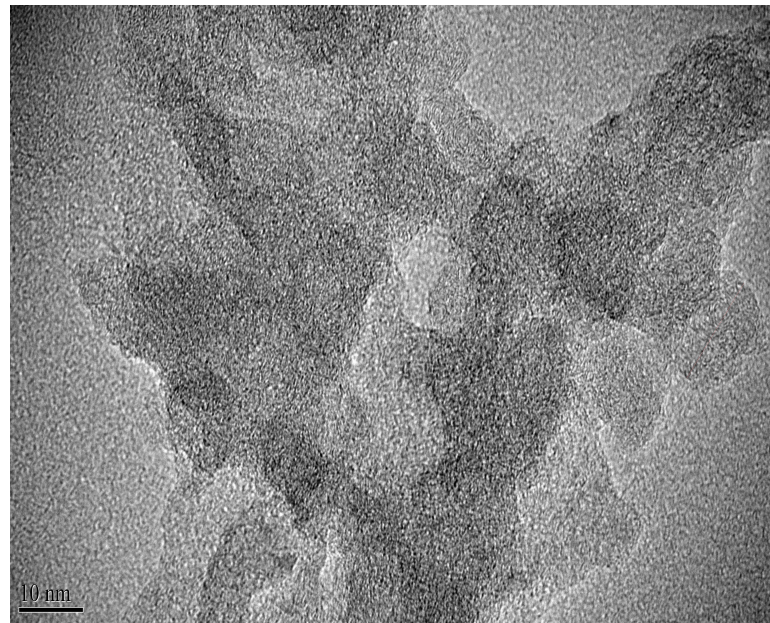


Figure 4.13 HRTEM image of carbon nanoparticles synthesized at 4.1kV using graphite electrodes

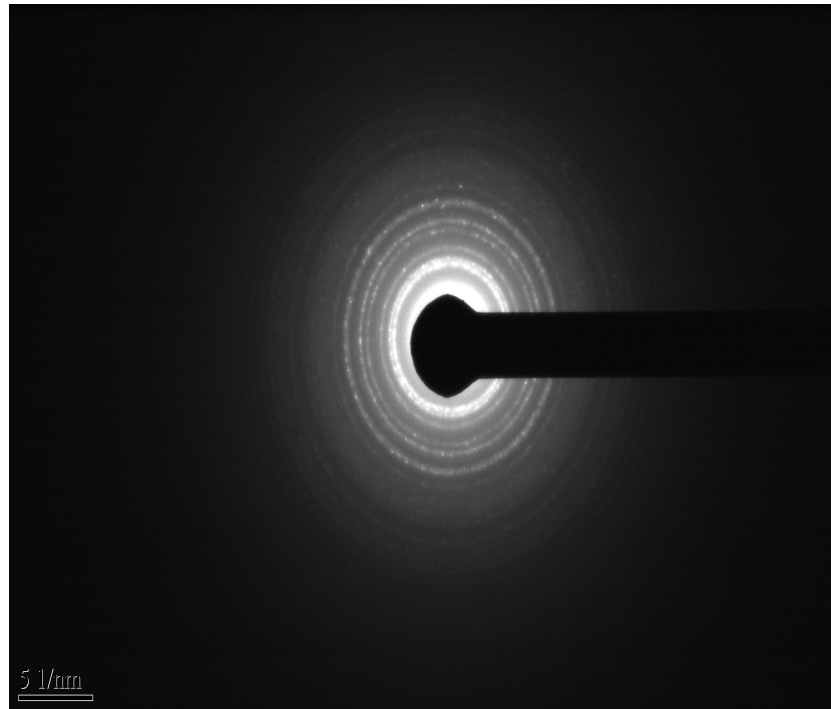


Figure 4.14 Diffraction pattern of CNP prepared at 4.1kV with graphite electrodes

Table 4.3 Tabulated value of the d-spacing as calculated from Figure 4.14

	d1	d2	d3	d4	d5
Interplanar spacing	0.248nm	0.212nm	0.172nm	0.162nm	0.141nm

Table 4.3 shows the interplanar spacing (d1, d2) were calculated by using the following relation

$$dD / 2 = \lambda L$$

Where, d=interplanar spacing, D=diameter of diffraction rings, λ =wavelength and L=camera length. Comparing these interplanar spacing it was found that the carbon nanoparticles formed were i-carbon form of carbon.

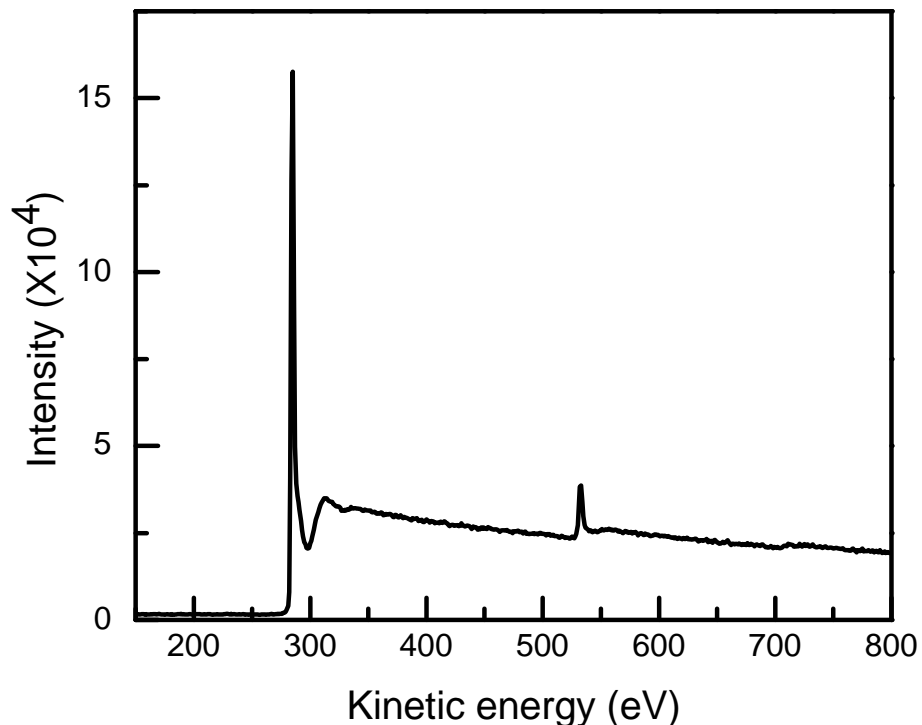


Figure 4.15 X-ray photoelectron spectroscopy of the nanoparticles synthesized using carbon electrodes

Figure 4.15 shows the elements present in the powder sample obtained by XPS analysis. It shows the presence of carbon and oxygen, at 285eV and 530 eV respectively. The amount of iron in the Fe-CNPs is very small so it is not traced by the XPS system.

Raman spectrum of the CNP's is shown in Figure 4.15. It can be seen that the spectrum resembles more that of a mostly amorphous graphite powder [18].

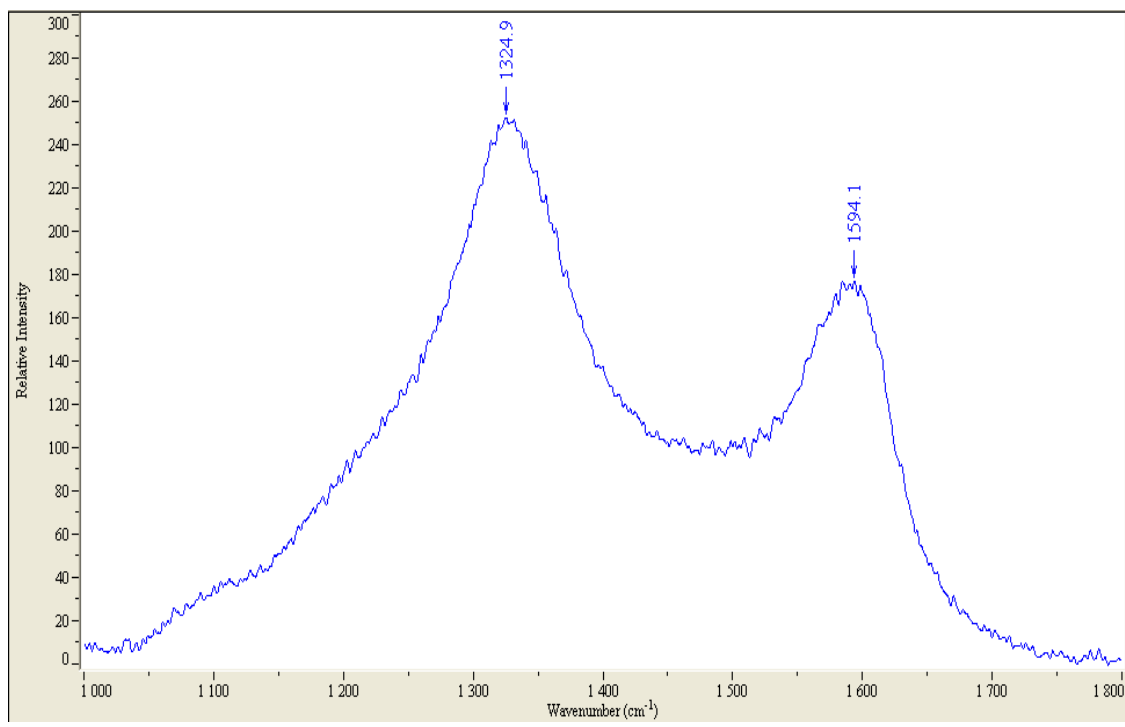


Figure 4.16 Raman spectroscopy of CNP synthesized at 4.1kV using graphite electrodes

CHAPTER 5

CONCLUSIONS

Magnetic carbon nanoparticles have been synthesized by a new method in which ultrasonic cavitation caused plasma discharge between two closely placed electrodes. This novel method uses relatively low level of electric power and is applicable in insulating organic solutions. The bubbles produced in the solvent via ultrasonic waves grow to a certain size before imploding resulting in high local temperature and pressure. This provides a conducting path between the electrodes and the atoms sublimate resulting in formation of the Fe-CNPs. The NPs produced in this way ranged in size from 5 to 40 nm in diameter. Their crystalline cores were spherical in shape, surrounded by tightly wrapped onion graphitic layers. Selected area electron diffraction pattern was used to find out the different forms of carbon and other products. Spacing between the fringes was in the range of 1.8 \AA^0 to 3.5 \AA^0 . EDX results confirmed the presence of iron which was in very less amount (~3% atomic concentration). The synthesized powder was superparamagnetic at room temperature in an applied magnetic field of 10000 Oe. The values of saturation magnetization can be increased by increase the operating voltage. The magnetic properties of the various samples mentioned in this thesis have been summarized in Table 5.1.

Table 5.1 Magnetic properties of various nanoparticles with and without the metallic core

Carbon nanoparticles	Remanence(M_r/M_s)	Coercivity
Graphite electrode at 4.1kv	0.154	200 Oe
Iron electrode at 3.7 kV	0	0
Iron electrode at 4.1kv	0	0

These differences are probably due to the nano scale structure of the synthesized powder and the proportion of non-magnetic phases. Raman spectroscopy was carried out to ascertain the bonding in the carbon phase of the NPs. The Raman spectra of Fe-CNP produced at 3.7 kV and CNP produced at 4.1 kV show broad D and G bands. An interesting observation was that the Fe-CNP synthesized at 4.1 kV have Raman spectrum very similar to that of diamond particles suggesting that the Fe-CNP are nano-diamond like. Initial absorption studies suggest that the Fe-CNP produced via this method have good absorption property at 1065 nm and hence could have biomedical application.

REFERENCES

- [1] Ruslan Sergienko, Etsuro Shibata, Akase Zentaro, Daisuke Shindo, Takashi Nakamura, Gaowu Qin, Formation and characterization of graphite-encapsulated cobalt nanoparticles synthesized by electric discharge in an ultrasonic cavitation field of liquid ethanol, *Acta Materialia* 55 (2007) 3671–3680.
- [2] Ruslan Sergienko, Etsuro Shibata, Zentaro Akase, Hiroyuki Suwa, Takashi Nakamura, Daisuke Shindo, Carbon encapsulated iron carbide nanoparticles synthesized in ethanol by an electric plasma discharge in an ultrasonic cavitation field, *Materials Chemistry and Physics* 98 (2006) 34–38.
- [3] J. Borysiuk, A. Grabias, J. Szczytko, M. Bystrzejewski, A. Twardowski, H. Lange, Structure and magnetic properties of carbon encapsulated Fe nanoparticles obtained by arc plasma and combustion Synthesis, *C A R B O N* 46 (2008) 1693–1701.
- [4] Jose' Luis Corchero, and Antonio Villaverde, Biomedical applications of distally controlled magnetic nanoparticles, *Trends in Biotechnology* Vol.27 No.8
- [5] M.R. Ibarra, R. Fernández-Pacheco, C. Marquina, D. Serrate and J.G Valdivia, Biomedical applications based on magnetic nanoparticles, European School of Magnetism : New experimental approaches to Magnetism - Constanta, 2005
- [6] B J Panessa-Warren, JBWarren, S S Wong and J A Misewich, Biological cellular response to carbon nanoparticles Toxicity, *J. Phys.: Condens. Matter* 18 (2006) S2185–S2201
- [7] R Jurgons, C Seliger, A Hilpert, L Trahms, S Odenbach and C Alexiou, Drug loaded magnetic nanoparticles for cancer therapy, *J. Phys.: Condens. Matter* 18 (2006) S2893–S2902

- [8] Linfeng Chen, Jining Xie, Justin Yancey, Malathi Srivatsan, and Vijay K. Varadan, Magnetic Nanoparticles and Nanotubes for Biomedical Applications, Proc. of SPIE Vol. 7291 729108-1.
- [9] Ch. Alexiou, A. Schmidt, R. Klein, P. Hulin, Ch. Bergemann, W. Arnold, Magnetic drug targeting: biodistribution and dependency on magnetic field strength, Journal of Magnetism and Magnetic Materials 252 (2002) 363–366.
- [10] Q A Pankhurst, J Connolly, S K Jones and J Dobson, Applications of magnetic nanoparticles in biomedicine, J. Phys. D: Appl. Phys. 36 (2003) R167–R181
- [11] Roca, R Costo, A F Rebolledo, S Veintemillas-Verdaguer, P Tartaj, T González-Carreño, M P Morales and C J Serna, Progress in the preparation of magnetic nanoparticles for applications in biomedicine, J. Phys. D: Appl. Phys. 42 (2009) 224002 (11pp)
- [12] Rodrigo Fernández-Pacheco, Manuel Arruebo, ClaraMarquina, Ricardo Ibarra1, Jordi Arbiol3 and Jesús Santamaría, Highly magnetic silica-coated iron nanoparticles prepared by the arc-discharge method, Nanotechnology 17 (2006) 1188–1192
- [13] Chenjie Xu and Shouheng Sun, Monodisperse magnetic nanoparticles for biomedical applications, Polym Int 56:821–826 (2007)
- [14] M Horton, A Khan and S Maddison, Delivering nanotechnology to the healthcare, IT and environmental sectors a perspective from the ‘London Centre for Nanotechnology’, BT Technology Journal, Vol 24 No 3, July 2006
- [15] Tobias Neuberger, Bernhard Schöpf, Heinrich Hofmann, Margarete Hofmann, Brigitte von Rechenberg, Superparamagnetic nanoparticles for biomedical applications, Possibilities and limitations of a new drug delivery system, Journal of Magnetism and Magnetic Materials 293, (2005), p483–496.

- [16] Jin Ho Bang and Kenneth S. Suslick, "Applications of Ultrasound to the Synthesis of Nanostructured Materials", Advanced Materials, 2010, 22, 1039–1059.
- [17] K.S. Suslick, S.J. Doktycz and E.B. Flint, On the origin of sonoluminescence and sonochemistry, Ultrasonics 1990, Vol 28, September.
- [18] Ruslan Sergiienko et. al., Materials Chemistry and Physics Volume 98, Issue 1, 1 July 2006, Pages 34-38.
- [19] B.D. Josephson, Phys. Letters 1, 251, 1962
- [20] J.C. Gallop SQUIDs, The Josephson Effect and Superconducting Electronics (Adam Hilger, 1991)
- [21]. S.S. Swithenby SQUIDs and their applications in the measurement of weak magnetic fields. J Phys E: Sci. Instrum. 1980, 13:801-813.
- [22] Jong Hyun Choi et al. Nano Letters, 2007, 7(4), pp 861-867

BIOGRAPHICAL INFORMATION

Sunilsingh Gusain was got his primary education from Kendriya Vidyalaya High School at Baroda, Gujarat-India. He earned his Bachelor of Engineering degree in Metallurgy Engineering from Maharaja Sayajirao University at Baroda, Gujarat-India in 2005. In fall 2007, he joined University of Texas at Arlington in the Material Science and Engineering department to pursue a Master of Science degree. He conducted research under Prof. A. R. Koymen.